ACS OMEGA

Open Access

http://pubs.acs.org/journal/acsodf

Article

Heterostructured S-Scheme BiOBr/Cu_2O Nanocomposite for Photocatalytic Degradation of Glyphosate

Albert Gonzalez,[#] Abelline Fionah,[#] Gbemisola J. Bamiduro,[#] and Elsayed M. Zahran*

Cite This: *ACS Omega* 2024, 9, 48512−48523

Read Online

ACCESS | Metrics & More | Article Recommendations | Supporting Information

ABSTRACT: Metal oxide semiconductor-activated photocatalysis has become a promising sustainable technology for the mitigation of emerging organic pollutants. The rational design of a photocatalyst heterojunction allows the degradation of a broad range of organic contaminants. Herein, we optimized hydrothermal approaches for the facial synthesis of well-defined BiOBr/Cu_2O heterojunction photocatalysts. Tuning the synthesis condition enhanced the interfacing of BiOBr and Cu_2O nanostructures in the heterojunction photocatalyst, as confirmed by STEM, TEM, XPS, XRD, and BET analysis. The optimized BiOBr/Cu_2O heterostructured photocatalyst demonstrated substantial activity in the degradation of both anionic and cationic dyes compared to the individual components. The enhanced nanocomposite exhibited complete degradation of glyphosate in 10 min of light irradiation and demonstrated high stability after five photocatalytic cycles. Our mechanistic and photoelectrochemical studies suggest that establishing an S-scheme heterojunction between BiOBr and Cu_2O enhances the separation of photogenerated charge carriers and expands the redox potentials of the nanocomposite to allow high catalytic efficiency. These findings indicate that tuning the design of metal oxide heterojunctions promises applications in the remediation of a wide range of organic contaminants.

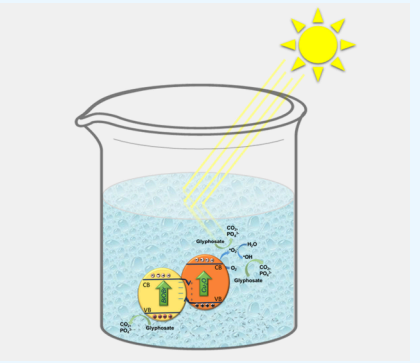

1. INTRODUCTION

Energy demand and industrialization have been increasing rapidly, resulting in significant contamination of the environment.[1] Emerging organic contaminants (EOC) have recently been recognized as a threat to human health and ecosystems.[2] For instance, glyphosate—a widely used nonselective herbicide—has been linked to several adverse effects on human health, including cancer and kidney and liver diseases.[3−5] High levels of glyphosate have been found mostly in runoff water sources, with residues found in various food products.[6,7] Aminomethylphosphonic acid (AMPA) is the primary degradation product of glyphosate, and studies have demonstrated that it is more persistent in the environment.[8,9] Therefore, environmentally friendly and cost-effective approaches for the remediation of glyphosate contamination in wastewater have recently garnered much interest.

Metal oxide semiconductor photocatalysts can harness solar energy for sustainable applications in renewable energy, hydrogen generation, and degradation of organic pollutants.[10−13] However, the widespread application of this technology is limited by insufficient visible light absorbance, electron−hole recombination, and incompatibility of the catalyst with reactants. Most research focuses on creating various types of heterojunctions to enhance electron−hole separation and improve the charge carriers' kinetics. Interfacing visible-light absorbing metal oxides, such as Cu_2O, Fe_2O_3, and $BiVO_4$ with TiO_2 and ZnO, has demonstrated an effective approach to increase the solar light harnessing of the heterostructured photocatalysts.[14−16] However, the rational design of heterojunction photocatalysts to leverage the interplay between the material's surface charges and organic contaminant polarity remains a formidable challenge. Copper(I) oxide (Cu_2O) has garnered much attention recently as a visible light-activated metal oxide photocatalyst because of its high abundance, environmentally benign nature, and narrow band gap of ∼2.2 eV.[17−19] Cubed and octahedral crystal-shaped Cu_2O have demonstrated excellent activity in the photocatalytic degradation of various organic contaminants.[20,21] However, as an independent photocatalyst, Cu_2O suffers from low photostability, a high rate of electron−hole recombination, and slow charge carrier transfer.[22,23] Therefore, the formation of heterojunctions incorporating Cu_2O with other semiconductors has been investigated to increase its photostability and photocatalytic activity.[24] However, most of these heterojunctions were designed to tune the band gap of a semiconductor and reduce the electron/hole recombination rates.[25,26] For instance, Hu et al. synthesized a Cu_2O/CeO_2 heterojunction that demonstrated improved activity in the

Received: August 8, 2024
Revised: October 25, 2024
Accepted: October 30, 2024
Published: November 21, 2024

photocatalytic degradation of acid orange, which was attributed to a reduced rate of electron−hole recombination.[27]

Bismuth oxyhalides (BiOX, X = Cl, Br, I) have demonstrated promising photocatalytic activity in the degradation of organic pollutants and photoelectrochemical applications.[28,29] Bismuth oxybromide (BiOBr) photocatalysts exhibit a nanolayered structure with a Bi_2O_2 slab cross-linked with two layers of Br^- creating an internal electric field that efficiently separates electrons and holes. In the meantime, the orientation of the Br^- slabs toward the surface of the material enhances the adsorption of cationic organic contaminants. As such, BiOBr has demonstrated potential for the design of heterojunction photocatalysts with high activity. For instance, Palmai et al. demonstrated an enhanced degradation of rhodamine B and polychlorinated biphenyls (PCBs) using $BiVO_4$/BiOBr heterojunction photocatalyst.[30]

The Step-Scheme (S-Scheme) heterojunction has garnered much attention in the past decade as an alternative band alignment with enhanced charge carriers separation and strong redox potentials for efficient photocatalytic reactions.[31] The S-scheme heterojunction comprises a reduction photocatalyst (RP) and an oxidation photocatalyst (OP) arranged in a staggered band alignment. In this configuration, the potentials of the conduction band (CB), valence band (VB), and Fermi levels of the RP are more electronegative than those of the OP. Under light excitation, the resulting potential difference generates an internal electric field at the interface, which facilitates the recombination of photogenerated charges with weak redox potentials—specifically, electrons at the OP CB and holes at the RP VB—thereby enabling those with strong redox potential to perform efficient photocatalytic reactions.[31] For instance, S-scheme heterojunction photocatalysts, such as WO_3/g-C_3N_4, CdS-TiO_2, and BiOBr/COF, demonstrated enhanced photocatalytic rates in hydrogen generation via photoelectrochemical water splitting, CO_2 reduction, and degradation of organic pollutants.[32−34] Thus, creating an S-scheme heterojunction between BiOBr and Cu_2O increases the visible light absorption of the composite, enhances the separation of charge carriers, promotes the redox power of the photocatalyst, and allows the adsorption of a broad range of organic contaminants.

Herein, we designed an S-scheme BiOBr/Cu_2O heterojunction photocatalyst using one-pot facial surfactant-assisted methods at relatively low temperatures. The reaction conditions were rationally optimized to control the morphology and composition of the composite material and enhance the interfacial interaction between the two oxides in the composite material. The BiOBr/Cu_2O heterostructured nanocomposite demonstrated effective degradation of both organic dyes. Furthermore, the BiOBr/Cu_2O photocatalyst displayed substantial photocatalytic activity in the light-activated degradation of glyphosate and AMPA. These results provide a unique approach to designing heterostructured photocatalysts with improved charge carrier transportation and optimized surface interaction for the degradation of a wide range of organic pollutants.

2. MATERIALS AND METHODS

2.1. Chemicals. High-purity cupric sulfate, sodium carbonate, cupric acetate, sodium sulfite, L-ascorbic acid, and sodium sulfate were obtained from Fisher Scientific (FairLawn, NJ). Bismuth(III) nitrate hydrate, rhodamine B (RhB), and methyl orange (MO) were acquired from Alfa Aesar (Ward Hill, MA). Cetyltrimethylammonium bromide (CTAB) was purchased from Chem−impex − Int'l Inc. (Wood Dale, IL). Sodium hydroxide, glyphosate, sodium bicarbonate, aminomethylphosphonic acid (AMPA), 2-proponal, sodium phosphate monobasic monohydrate, and potassium phosphate dibasic were obtained from Sigma-Aldrich (St. Louis, MO). Dextrose was acquired from VWR Chemicals (Radnor, PA), and hydrazinium hydroxide was purchased from Merck KGaA (Darmstadt, Germany). Ethyl alcohol (ACS/USP grade, 190 proof) was obtained from Pharmaco−Aaper (Toronto, Ontario). High-purity deionized water (18.2 MΩ•cm) filtered with Barnstead NanoPure by Thermo Sceintific was used for all experiments.

2.2. Characterization. High-resolution transmission electron microscopy (HRTEM ≤ 0.10 nm)) and scanning transmission electron microscopy (STEM ≤ 0.16 nm) images were obtained with a FEI Talos F200X operating at 200 kV equipped with a Super−X EDS system with 4 FEI-designed Silicon Drift Detectors. N_2−BET adsorption−desorption specific surface area analysis was performed with the Quantachrome autosorp iQ−C−AG/MP/XR. Diffuse reflectance spectroscopy (DRS) was performed on a Shimadzu UV−2600 spectrophotometer (200−800 nm). X-ray crystallography data for all materials was obtained using the Rigaku benchtop Mini Flex 600 X-ray diffractometer (XRD) with Cu Kα radiation. The X-ray photoelectron spectroscopy (XPS) analysis was performed using a PHI Versa Probe II with monochromatic Al Kα X-ray and a power source of 25 W at 15 kV coupled with an 8×10^{-10} Torr ca. base pressure and a 45° take of angle and a 100 μm beam size at the X-ray incidence. Photoluminescence (PL) studies were conducted with the Jasco FP−8350 spectrofluorometer (200 to 800 nm).

2.3. Photocatalyst Synthesis. *2.3.1. Synthesis of BiOBr.* The BiOBr photocatalyst was prepared according to our previous report with some modifications.[9] Briefly, 365 mg of CTAB was dissolved in 20 mL of DI water at 60 °C. Separately, 970 mg of $Bi(NO_3)_3{\cdot}5H_2O$ was dissolved in 10 mL of DI water at room temperature and left stirring for 10 min to generate a white suspension. Afterward, the as-prepared white suspension was added dropwise into the CTAB solution and left stirring under reflux at 80 °C overnight. The as-prepared product was cooled to room temperature, collected via vacuum filtration, and washed several times with Millipore water and 190-proof ethanol. It was then dried overnight in a vacuum oven at 60 °C.

2.3.2. Synthesis of Cu_2O. 365 mg of CTAB was dissolved in 100 mL of a 0.1 M copper(II) acetate solution. Then, 50 mL of a 0.1 M NaOH solution was added dropwise. The solution was then heated to 60 °C for 15 min. Afterward, 50 mL of a 0.1 M hydrazine hydrate solution was added to the warm solution. The solution was heated for 20 min under stirring, and then for an additional 10 min without stirring. The synthesized material was washed several times, filtered, and dried in the vacuum oven overnight.

2.3.3. Synthesis of BiOBr/Cu_2O. Three synthetic methods were explored to prepare BiOBr/Cu_2O heterojunction with optimal interfacing between the two oxides.

Method A. 365 mg of CTAB and 970 mg of $Bi(NO_3)_3{\cdot}5H_2O$ were added into a 250 mL round-bottom flask containing 100 mL of a 0.05 M $CuSO_4$ solution at room temperature. After the complete dissolution of the materials, 12.5 mL of a 1 M NaOH solution was added dropwise into the round-bottom flask. Subsequently, 30 mL of 1 M dextrose

https://doi.org/10.1021/acsomega.4c07304
ACS Omega 2024, 9, 48512−48523

solution was injected dropwise into the reaction mixture. The round-bottom flask was then placed in an oil bath maintained at 80 °C for 2 h. The product was then cooled off to room temperature, filtered via vacuum filtration, and washed twice with Millipore water and once with 190-proof ethanol. It was then dried overnight in a vacuum oven at 60 °C.

Method B. In a two-neck 250 mL round-bottom flask, 365 mg of CTAB and 970 mg of $Bi(NO_3)_3{\cdot}5H_2O$ were dissolved in 100 mL of a 0.1 M copper (ii) acetate solution. Subsequently, 50 mL of a 0.1 M NaOH solution was added dropwise into the flask with continuous stirring. The solution was then heated to 60 °C for 15 min, and 50 mL of a 0.1 M hydrazine hydrate solution was added dropwise to the flask. The reaction mixture was maintained at 60 °C for 20 min with continuous stirring and an additional 10 min without stirring. The product was collected by vacuum filtration and dried as described above.

Method C. In a two-neck 250 mL round-bottom flask, 25 mL of 0.1 M $Bi(NO_3)_3{\cdot}5H_2O$ was added dropwise to 25 mL of a 0.1 M solution of CTAB in an oil bath maintained at 80 °C, with the contents left to stir for 2.5 h. Afterward, 100 mL of a 0.1 M copper (ii) acetate solution was added dropwise to the flask. Subsequently, 50 mL of a 0.2 M NaOH solution was added dropwise to the reaction mixture in the flask. The reaction mixture was maintained at 60 °C for 20 min with continuous stirring and an additional 10 min without stirring. The product was collected by vacuum filtration and dried as described above.

2.4. Photoelectrochemical Characterization. The photoelectrodes were prepared according to our previously reported method with some modifications.[35] Briefly, fluorine-doped tin oxide (FTO, Techinstro, Maharashtra, India) substrates were cleaned by ultrasonication in DI water and then acetone. One-half of the FTO glass substrate was masked using adhesive tape. Aqueous slurries of the $BiOBr/Cu_2O$ materials were prepared by dissolving 20 mg in 0.5 L of 0.5% Nafion diluted by a 1:1 ratio of ethanol and DI water followed by sonication for 30 min. The prepared slurry was deposited on the exposed FTO glass and dried in the oven at 60 °C for 120 min. After drying and cooling, the remaining space was covered with nonconductive epoxy, and a 1 mm space at the edge was covered with conductive silver epoxy (Electron Microscopy Sciences, Hatfield, PA) to make the electrical connection to the potentiostat. The photocurrent measurements were measured by an electrochemical analyzer (Autolab PGSTAT30 Potentiostat) in a standard three-electrode system with the photocatalyst as the working electrode, a Pt coil filament as the counter electrode, and an Ag/AgCl as the reference electrode. An Oriel light source with a 300 W Xe arc lamp was used for light illumination. All photoelectrochemical measurements were conducted in 0.1 M Na_2SO_4 solution adjusted to pH 6.9 with a NaH_2PO_4/Na_2HPO_4 solution as a supporting electrolyte. The measurements for transient photocurrent response were performed while maintaining a constant applied potential of 1.2 V vs Ag/AgCl. The electrochemical impedance spectroscopy (EIS) measurements were conducted while the sample was under light illumination with a sinusoidal wave amplitude of 100 mV over a frequency range from 1 Hz to 500 kHz with an open-circuit potential. The impedance data were fitted to the equivalent circuit using the Randles model. Finally, linear sweep voltammetry (LSV) measurements were performed under light irradiation at potentials ranging from 0.5 to 2.0 V versus Ag/AgCl with a scan rate of 0.5 V/s.

2.5. Photocatalytic Degradation of Rhodamine B and Methyl Orange. The photocatalytic experiments were carried out using a 300 W xenon lamp with 100 mW/cm^2 optical power output. The photocatalytic activity of the $BiOBr/Cu_2O$ heterojunction and its components was first evaluated in the presence of cationic and anionic model organic dyes, rhodamine B and methyl orange, respectively.

In a typical rhodamine B (RhB) or methyl orange dye degradation experiment, a specific amount of the photocatalyst was dispersed in 20 mL of 20 μM dye in a 100 mL quartz reactor. The solution was left to stir in the dark for 30 s to attain an adsorption−desorption equilibrium. This was followed by irradiation with the solar simulator with subsequent collection of 600 μL aliquots at selected time intervals. The aliquots were centrifuged to remove the catalyst particles, and a Shimazu UV1800 UV−vis spectrophotometer was used to quantify the dye concentration.

2.6. Photocatalytic Degradation of Glyphosate and AMPA. The optimized $BiOBr/Cu_2O$ heterojunction photocatalyst and the individual components were utilized in the photocatalytic degradation of glyphosate (GLP) and aminomethylphosphonic acid (AMPA). In a typical GLP or AMPA degradation experiment, 60 mg of the photocatalyst was dispersed in 60 mL of 50 μM solution of GLP or AMPA in a 100 mL quartz reactor. To establish an adsorption−desorption equilibrium, the mixture was subjected to stirring in the dark for 30 s. The light was subsequently turned on and 1 mL aliquots were taken at specific time intervals for 1 h. The catalyst particles were removed from the sample by centrifugation, and then 600 μL was transferred to a 2 mL autosampler vial for analysis of glyphosate and AMPA using a Dionex ICS − 5000 system (Thermo Fisher Scientific) high-performance liquid chromatography ion-chromatography (HPLC − IC). The separation was performed with a Dionex Ion Pac AS22 analytical column (250 mm × 2 mm × 4 μm) and Dionex Ion Pac AG22 guard column (50 mm × 2 mm × 4 μm). The temperature of both the column and detector was set at 35 °C. The injection volume was 20 μL. The glyphosate and degradation products were separated by an isocratic elution of 4.5 mM Na_2CO_3/ 1.4 mM $NaHCO_3$ buffer solution with a flow rate of 1.2 mL/min. An AERS 500 Carbonate suppressor (4 mm) was used and set at 31 mA to reduce the background signal from the mobile phase.

The stability of the optimized $BiOBr/Cu_2O$ material was evaluated in the degradation of glyphosate for 5 consecutive cycles. During each reaction cycle, 1 mL aliquots were taken and centrifuged at selected time intervals. The solution was stirred for an additional 50 min to remove any carbonaceous residues from the material active sites. After the completion of each cycle, 2 mL of glyphosate was added to the reaction mixture for the subsequent cycle.

To investigate the photocatalytic mechanism of the $BiOBr/Cu_2O$ photocatalyst, various radical scavengers such as sodium sulfite (SSI), ascorbic acid (AA), and isopropyl alcohol (IPA) were utilized in the degradation of 10 mg/L of both rhodamine B and methyl orange. The samples were similarly analyzed with UV−vis spectroscopy. Furthermore, glyphosate degradation was evaluated similarly, with the use of an HPLC-IC as described previously.

To observe the degree of mineralization, total organic carbon (TOC) analysis was performed with a Shimadzu TOC−L CPH, and molybdenum blue analysis was conducted to monitor phosphate formation.

https://doi.org/10.1021/acsomega.4c07304
ACS Omega 2024, 9, 48512−48523

3. RESULTS AND DISCUSSION

3.1. Characterization. Three low-temperature hydrothermal synthetic approaches (**A**, **B**, and **C**) were investigated to develop BiOBr/Cu_2O heterostructured photocatalysts with significant intercalation between the two metal oxides. The BiOBr/Cu_2O heterojunction nanocomposites (**A** to **C**) and the bare BiOBr and Cu_2O nanomaterials were characterized by electron microscopy to analyze their morphology, size, and architecture. The TEM images in Figure 1a show that the bare BiOBr nanomaterial exhibits a layered structure with aggregated platelike nanosheets with an average diameter of 0.43 ± 0.05 μm. Figure 1b shows that the Cu_2O nanomaterial forms well-defined hollow cubes with an average size of 114 ± 14 nm. For the BiOBr/Cu_2O heterojunction nanocomposite prepared by method **B** (BiOBr/Cu_2O (**B**)), the TEM micrographs in Figure 1c,d display Cu_2O polyhedra integrated with the BiOBr nanosheets (average diameter of 0.43 ± 0.08 μm). The Cu_2O materials evolved into a hollow polyhedral shape,[36] and the particles exhibited an increased average width of 166 ± 41 nm, which can be attributed to the influence of the heterojunction formation (Figure 1d). Moreover, high-resolution TEM (HR-TEM) analysis of the (BiOBr/Cu_2O (**B**)) heterojunction demonstrates clear lattice fringes (Supporting Information, Figure S1), which expresses a stacked and uniform composition of the crystallized BiOBr component integrated with Cu_2O nanostructures. On the other hand, the TEM image of the nanocomposite prepared by method **A** (BiOBr/Cu_2O (**A**)) displayed uneven spheres with limited integration between Cu_2O nanostructures and BiOBr nanosheets (Supporting Information, Figure S2a). For nanocomposites prepared by Method **C** (BiOBr/Cu_2O (**C**)), the TEM images indicate a mixture of Cu_2O nanopolyhedra and BiOBr nanoplates in the composite material (Supporting Information, Figure S2b). These results demonstrate that the architecture, dimensions, and heterostructure of the different composite materials varied by the preparation method.

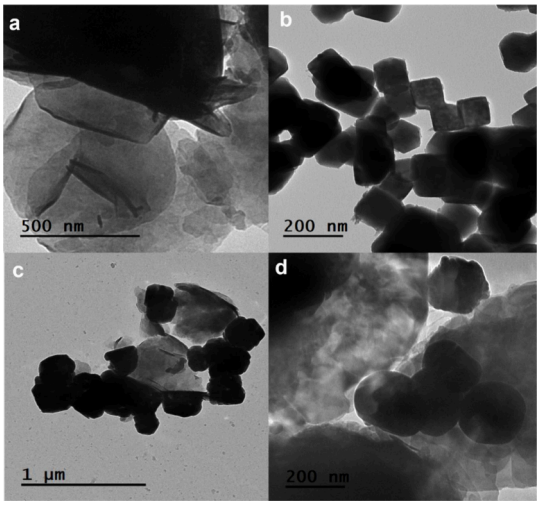

Figure 1. TEM analysis of (a) BiOBr, (b) Cu_2O, (c) BiOBr/Cu_2O (**B**) at 1 μm, and (d) BiOBr/Cu_2O (**B**) at 200 nm.

To confirm the elemental composition and ensemble of the heterojunction in the BiOBr/Cu_2O (**B**) composite material, high angular annular dark-field STEM (HAADF-STEM) images were obtained along with EDS elemental mapping. Figure 2b demonstrates a well-defined interface between the BiOBr and Cu_2O oxides in the BiOBr/Cu_2O (**B**) heterojunction nanocomposite. The EDS elemental mapping of the interface (Figure 2c–f) confirms the distribution of Bi, Cu, Br,

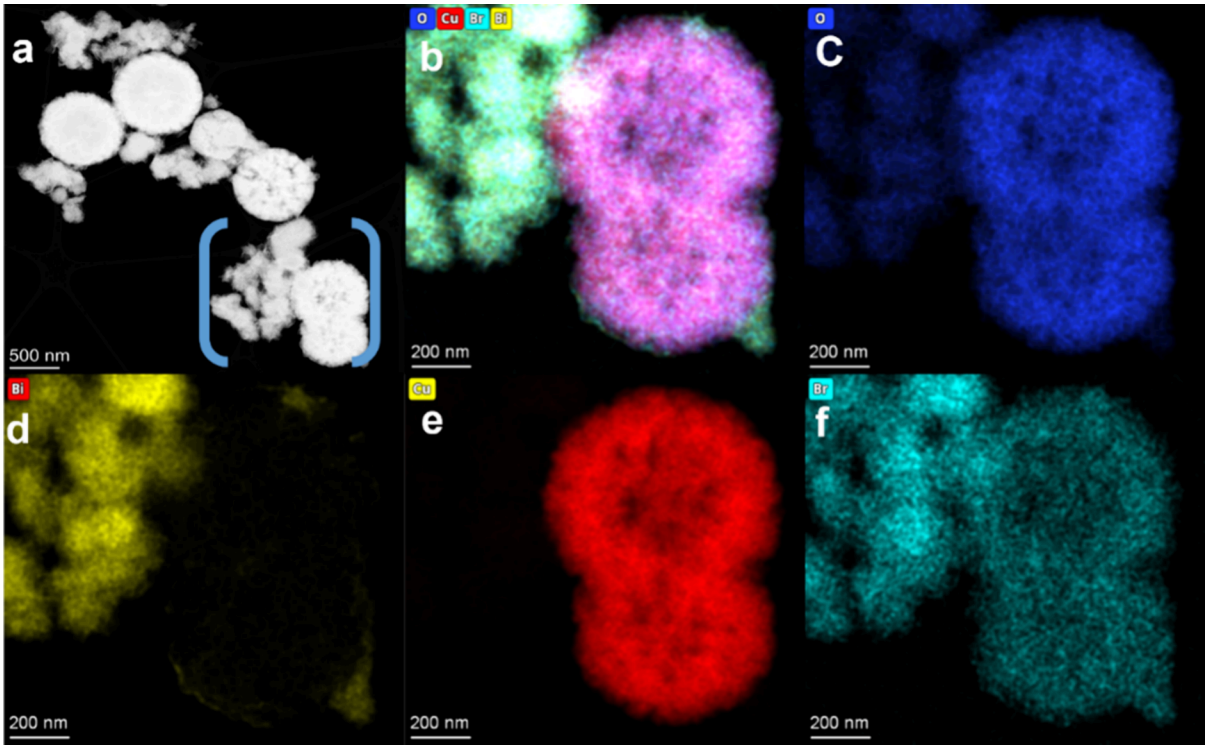

Figure 2. High-angle annular dark-field scanning transmission electron microscopy and EDS mapping analysis of the BiOBr/Cu_2O (**B**) material. (a) Presents the STEM image where EDS mapping of the region in the blue box is shown for the (b) composite, (c) O, (d) Bi, (e) Cu, and (f) Br.

https://doi.org/10.1021/acsomega.4c07304
ACS Omega 2024, 9, 48512−48523

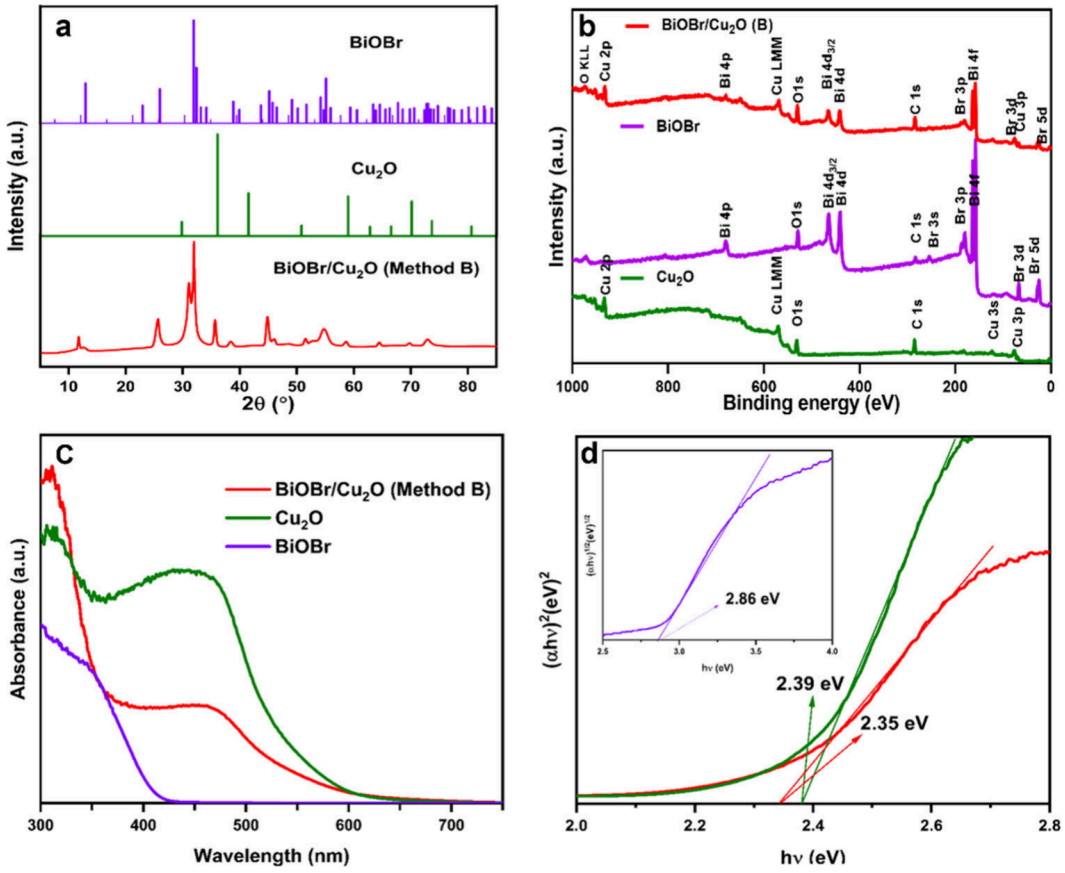

Figure 3. (a) XRD pattern of the BiOBr/Cu_2O (**B**) composite materials. (b) High-resolution XPS spectra of the BiOBr/Cu_2O (**B**) nanocomposite. (c) Diffuse reflectance UV−vis absorption of the BiOBr/Cu_2O (**B**) nanocomposite and individual materials. (d) Tauc plots of the composite and individual materials.

and O is consistent with the BiOBr/Cu_2O heterojunction nanocomposite. Further, the EDS spectra in Figure S3 display peaks for Bi, Cu, Br, and O with weight ratios matching the elemental composition of BiOBr/Cu_2O heterojunction photocatalyst.

The Brunauer−Emmett−Teller (BET) surface area was determined to evaluate the surface area of all the materials. Table S1 in the Supporting Information lists the BET surface area and pore volume of the individual components and composite materials. Figure S4a,b features their N_2−BET adsorption−desorption isotherm plot and the corresponding pore size distribution curves. All the materials exhibit mesoporous structures with Type IV isotherm hysteresis loop behavior at 0.4−0.8 P/P_0.[37] The bare BiOBr has the smallest surface area at 10.939 $m^2\ g^{-1}$ followed by the BiOBr/Cu_2O (**A**) with 11.539 $m^2\ g^{-1}$ and BiOBr/Cu_2O (**C**) with 12.145 $m^2\ g^{-1}$. However, the BET surface area of the bare Cu_2O material is 14.595 $m^2\ g^{-1}$, which is higher than the bare BiOBr and the method A and C composites. Notably, It is also higher than other previously reported surface areas for Cu_2O materials in the literature.[38] This can be attributed to the hollow nature of the Cu_2O nanostructures, as evident from the TEM images in Figure 1a. The same hollow structure is observed in the BiOBr/Cu_2O (**B**) composite material, which exhibited the highest surface area at 24.281 $m^2\ g^{-1}$. This result is further supported by the pore size distribution curves in Figure S4b, which show that the bare Cu_2O has a higher pore volume at 0.058 $cm^3\ g^{-1}$ than bare BiOBr at 0.032 $cm^3\ g^{-1}$. Thus, the BiOBr/Cu_2O (**B**) exhibits the highest pore volume at 0.063 $cm^3\ g^{-1}$. As such, the increased surface area and pore volume in composite **B**, when compared to pure BiOBr, stems from the combined surface areas and pore volume of the unique hollow Cu_2O nanostructures interfacing with the BiOBr nanosheets. This indicates that the BiOBr/Cu_2O (**B**) is best suited to adsorb various organic pollutants more effectively for enhanced photocatalytic activity.[39]

The nanocomposite materials were further characterized by powder X-ray diffraction (XRD) to identify their respective crystal phase structures. Figure 3a presents powder XRD patterns for composite material **B**, with all observed diffraction patterns of the nanocomposites demonstrating both tetragonal BiOBr (Card No. 1010421) and cubic/polyhedral Cu_2O (Card No. 1010963). In Figure 3a BiOBr reflections are observed at 2θ = 10.9, 32.1, 32.6, and 57.1°, while Cu_2O is demonstrated by reflections at 2θ = 29.6, 36.1, 56.5° for BiOBr/Cu_2O (**B**). In Supporting Information, Figure S5, the BiOBr/Cu_2O (**A**) material displays characteristic BiOBr and Cu_2O peaks at 2θ = 10.9, 32.6, 46.3° and 2θ = 61.4, 75.1°, respectively (Supporting Information, Figure S5). The BiOBr/Cu_2O (**C**) displays reflections at 2θ = 10.9, 32.6, 46.3° and 2θ = 36.5, 42.4, and 61.4°, demonstrating the presence of tetragonal phase BiOBr and cubed phase Cu_2O, respectively. The ratios of BiOBr to Cu_2O in the composites were calculated from the XRD spectra to be 68:32, 70:30, and 57:43 (wt/wt %) BiOBr/Cu_2O (**A**), BiOBr/Cu_2O (**B**), BiOBr/Cu_2O (**C**) nanocomposites, respectively.

The surface composition of the nanomaterials was further analyzed by X-ray photoelectron spectroscopy (XPS) to

https://doi.org/10.1021/acsomega.4c07304
ACS Omega 2024, 9, 48512−48523

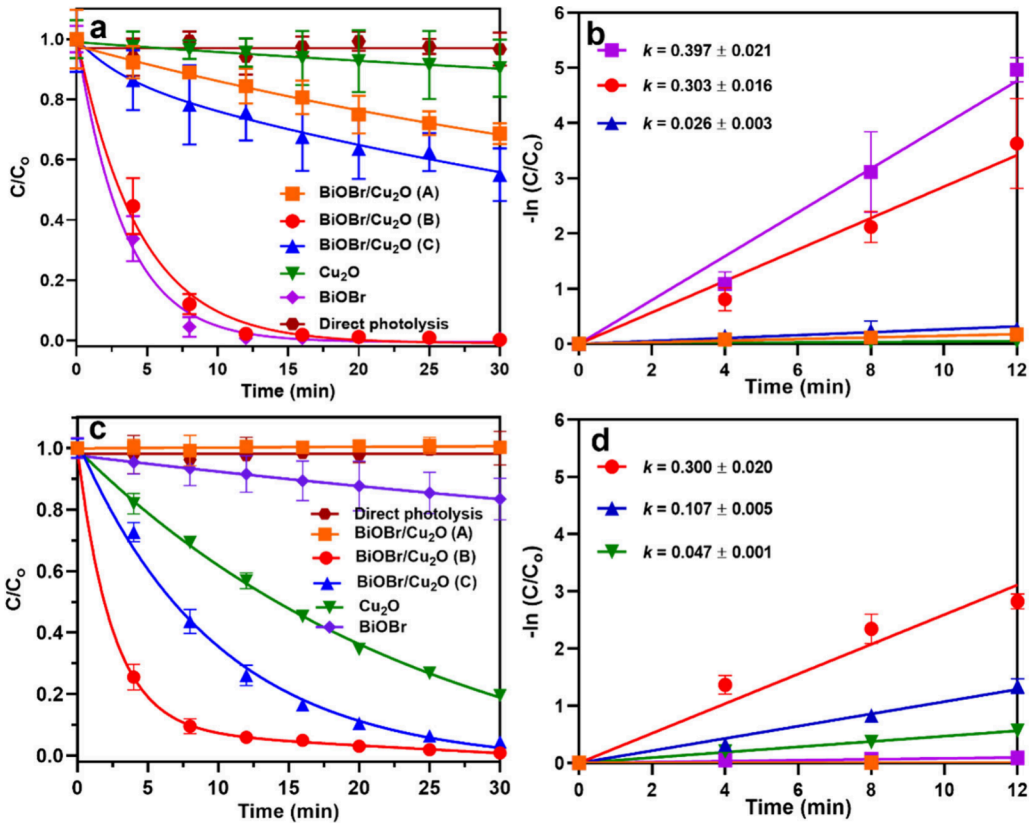

Figure 4. (a) Photocatalytic degradation of RhB versus time with BiOBr/Cu_2O (Method **A**−**C**) and the individual components as catalysts. (b) First-order rate for the photocatalytic degradation of RhB. (c) Photocatalytic degradation of MO versus time with BiOBr/Cu_2O (Method **A**−**C**) and the individual components as catalysts. (d) First-order rate for the photocatalytic degradation of MO.

confirm the oxidation states of the elements in the composite material. Based on the full XPS survey (Figure 3b), peaks for Cu and O were observed in the pure Cu_2O spectra, and peaks for Bi, O, and Br were observed in the pure BiOBr spectra. For the BiOBr/Cu_2O (**B**) composite, peaks for Bi, Br, Cu, and O were all present to confirm the heterojunction of the two components in the composite material. Figures S5a−d display the deconvoluted peaks of the individual elements in BiOBr/Cu_2O (**B**) nanocomposite. As shown in Figure S6a, the peaks at 158.5 and 164.0 eV for Bi $4f_{7/2}$ and Bi $4f_{5/2}$, respectively, confirm the presence of Bi^{3+} in the BiOBr/Cu_2O (**B**) sample, and the Br $3d_{5/2}$ peak at 68.1 eV (Figure S6b) demonstrates the presence of Br^- in BiOBr nanosheets. Figure S6c presents the Cu $2p_{3/2}$ peak at 931.5 eV and the Cu $2p_{1/2}$ peak at 951.3 eV, which can be attributed to Cu^+ for the BiOBr/Cu_2O (**B**) sample. XPS peak fitting (Figure S6c) revealed that the surface of the copper component consisted of 70.4% Cu^+ and 29.6% Cu^{2+}. Finally, Figure S6d presents the O 1s peak at around 529.9 and 531.8 eV, arising from Bi−O and Cu−O for BiOBr/Cu_2O (**B**).

The light absorption range and the band gaps of the materials were analyzed with UV−vis DRS to investigate the effect of the heterojunction. Figure 3c presents the UV−vis DRS spectra and their respective Tauc plots (Figure 3d) of the BiOBr/Cu_2O (**B**) sample and the bare BiOBr and Cu_2O photocatalysts. The BiOBr/Cu_2O photocatalyst exhibited a wider absorption range in the visible region than the pure BiOBr and Cu_2O. The band gap was determined from Tauc plots to be 2.86 and 2.39 eV for the bare BiOBr and Cu_2O photocatalysts, respectively. The heterojunction nanocomposites BiOBr/Cu_2O (**B**) exhibited reduced band gaps than the individual components at 2.35 eV. The bandgaps for BiOBr/Cu_2O (**A**) and BiOBr/Cu_2O (**C**) were 2.42 and 2.17 eV, respectively (Figure S7).

3.2. Photocatalytic Degradation of Rhodamine B and Methyl Orange. The rate-limiting step of the photocatalytic degradation of organic compounds by semiconductor nanocomposites is controlled by the adsorption of the contaminant molecules on the surface of the material. The extent of the adsorption depends on the surface charges of the photocatalyst and the charge of the organic contaminant. Bismuth oxyhalides photocatalysts have demonstrated substantial activity in the photocatalytic degradation of cationic dyes, such as rhodamine B, due to the orientation of the halide in the exposed crystal facet.[40,41] On the other hand, Cu_2O with copper ions on the surface facets has demonstrated excellent activity in the photocatalytic degradation of anionic dyes, such as methyl orange.[42,43] The BiOBr/Cu_2O heterojunction nanocomposites were designed to enable the photocatalytic degradation of a broad range of organic pollutants with various charges.[44] As such, the photocatalytic activity of the BiOBr/Cu_2O heterojunction nanocomposite was evaluated in the degradation of both RhB and MO dyes as model cationic and anionic organic pollutants, respectively. The three BiOBr/Cu_2O composites were employed in the degradation of both pollutants to optimize the synthesis method, resulting in the highest photocatalytic reactivity. For all the degradation reactions, insignificant changes in the dye concentration were observed after 30 min in the dark. Figure 4a shows the photocatalytic activities and rate constants of BiOBr, Cu_2O,

https://doi.org/10.1021/acsomega.4c07304
ACS Omega 2024, 9, 48512−48523

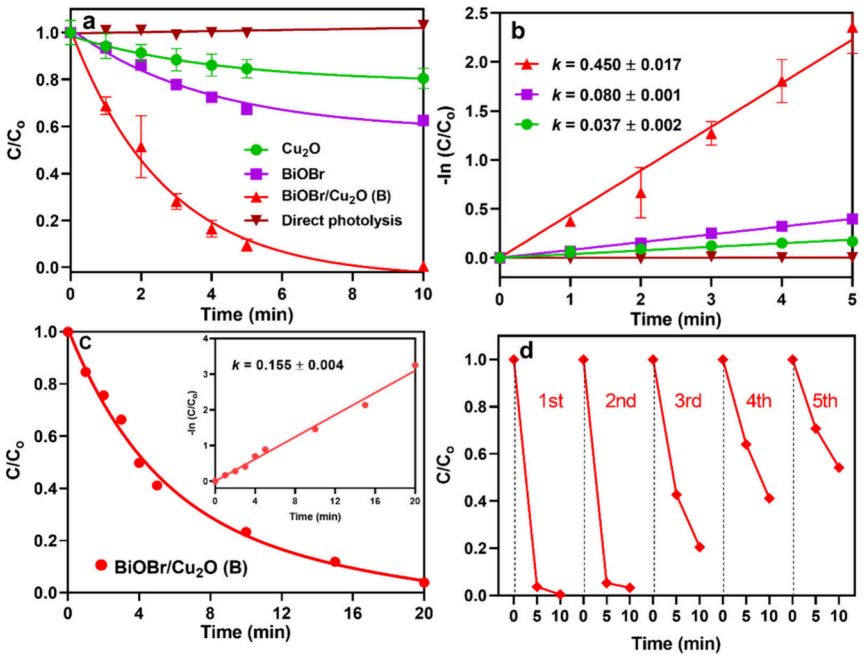

Figure 5. (a) Photocatalytic degradation of glyphosate versus time without catalyst and with BiOBr, Cu_2O, and BiOBr/Cu_2O (**B**) as catalysts. (b) First-order rate for the photocatalytic degradation of glyphosate. (c) Photocatalytic degradation of AMPA with BiOBr/Cu_2O (**B**) under light irradiation. (d) Stability analysis for BiOBr/Cu_2O (**B**) in the degradation of glyphosate.

and BiOBr/Cu_2O composites **A**–**C** in the photodegradation of the RhB dye as a function of irradiation time. For the control experiments, which were conducted in the absence of the composite material under light irradiation, and in the dark with the composites, the degradation of RhB was negligible. Conversely, significant degradation of RhB was observed in the presence of BiOBr photocatalyst. Complete degradation of the RhB dye by BiOBr nanosheets was achieved after 12 min of irradiation, while Cu_2O photocatalyst degraded only <5% of the dye after 12 min of light irradiation. On the other hand, the BiOBr/Cu_2O (**B**) nanocomposite demonstrated 100% degradation of the RhB dye in 12 min compared to 22% and 13% degradation for BiOBr/Cu_2O (**C**) and BiOBr/Cu_2O (**A**), respectively. The rate constants in Figure 4b were calculated and the k values were 0.397 ± 0.021 min^{-1} for BiOBr, 0.004 ± 0.005 min^{-1} for Cu_2O, 0.015 ± 0.001 min^{-1} for BiOBr/Cu_2O (**A**), 0.303 ± 0.019 min^{-1} for BiOBr/Cu_2O (**B**), and 0.026 ± 0.003 min^{-1} for BiOBr/Cu_2O (**C**).

Figure 4c illustrates the photocatalytic degradation of MO by the BiOBr/Cu_2O composite materials, individual components, and the control reactions. Control reactions were conducted to evaluate the degradation rate of MO with the materials in the dark and without the materials under light. All the control reactions demonstrated a negligible decrease in the MO concentration compared to the photocatalytic reaction in the presence of light. The bare BiOBr demonstrated low photocatalytic activity in the degradation of MO with ∼5% after 12 min of irradiation. On the other hand, the bare Cu_2O displayed a higher activity than bare BiOBr, with 40% of the MO dye degraded after 12 min. For the nanocomposite materials, the BiOBr/Cu_2O (**B**) demonstrated substantial activity by degrading 100% of the MO dye in 12 min with a rate constant of 0.300 min^{-1} compared to the BiOBr/Cu_2O (**A**) and BiOBr/Cu_2O (**C**) materials which demonstrated only 2% and 76%, reactivity toward the degradation of the MO dye in the same time frame. The rate constants k values in Figure 4d are 0.008 ± 0.001 min^{-1} for BiOBr, 0.047 ± 0.001 min^{-1} for Cu_2O, 0.004 ± 0.001 min^{-1} for BiOBr/Cu_2O (**A**), 0.107 ± 0.005 min^{-1} for BiOBr/Cu_2O (**C**), and 0.300 ± 0.198 min^{-1} for BiOBr/Cu_2O (**B**). The improved performance of the BiOBr/Cu_2O (**B**) photocatalyst might be attributed to the formation of the heterojunction that enhanced the separation of the charge carriers, reducing their recombination rate and facilitating their migration to the surface of the semiconductor. Furthermore, the improved activities of composite **B** can also be attributed to the combined activities of the cationic surface charge of Cu_2O nanostructured photocatalyst, which boosts its potency toward the degradation of negatively charged MO and anionic surface charge of BiOBr, which increases its potency toward RhB.[45,46] Besides, the increased BET surface area (Table S1) of the BiOBr/Cu_2O (**B**) composite also substantially enhances the diffusion path for the separated electrons/holes and the transfer of charge carriers. Thus, interfacing the two metal oxides in the BiOBr/Cu_2O (**B**) nanocomposite allows the catalytic reaction of organic contaminants with various charges on the surface of the catalyst resulting in the highest degradation efficiency for both RhB and MO dyes (Figure 4b, d). Moreover, the Cu_2O nanostructures exhibited polyhedral morphology (Figure 1) in the BiOBr/Cu_2O (**B**) heterojunction nanocomposite, suggesting decreased oxygen vacancies and contributing to improved photocatalytic activity. A similar phenomenon was observed by Plascencia et al., where a change in the morphology of the Cu_2O from cubes to polyhedrons resulted in improved activity.[36]

3.3. Photocatalytic degradation of Glyphosate.

According to the results of the photocatalytic dye degradation reactions, the BiOBr/Cu_2O (**B**) nanocomposite photocatalyst is adopted for the degradation of glyphosate and all further studies. Figure 5a displays the degradation of glyphosate by the individual components and BiOBr/Cu_2O (**B**) photocatalyst along with the control as a function of irradiation time. An

https://doi.org/10.1021/acsomega.4c07304
ACS Omega 2024, 9, 48512−48523

Table 1. Comparison of the Photocatalytic Performance of BiOBr/Cu_2O with Other Previously Reported Photocatalysts for the Degradation of Glyphosate in Recent Years

Photocatalysts	Catalyst dose	Reaction conditions	Degradation efficiency	Rate Constant (k)	refs.
CoS/BiOBr	0.4 g/L	200 mL 10×10^{-4} M + 44 W LED lamp	74.7% in 180 min	0.01 min^{-1}	50
$Bi_2S_3/BiVO_4$	0.4 g/L	500 mL 10×10^{-4} M + 125 W Hg lamp	79% in 180 min	-	51
$MoSe_2/BiVO_4$	0.2 g/L	500 mL 10×10^{-4} M + 125 W Hg lamp	86.1% in 180 min	-	52
CuS/Bi_2WO_6	0.4 g/L	80 mL 10×10^{-4} M + 44 W LED lamp	85.9% in 180 min	-	53
$BiOBr/Fe_3O_4$	4 g/L	20 mL 100 mg/L + 500 W Xe lamp	97% in 60 min	-	48
Citric acid/CeO_2	0.25 g/L	50 mL 25 mg/L + PCX-50 lamp	100% in 20 min	0.30 min^{-1}	54
$BiVO_4$/BiOBr	1 g/L	50 mL 50 mg/L + 300 W Xe lamp	100% in 6 min	0.29 min^{-1}	
Cu_2O/BiOBr	1 g/L	50 mL 50 mg/L + 300 W Xe lamp	100% in 10 min	0.45 min^{-1}	The present work

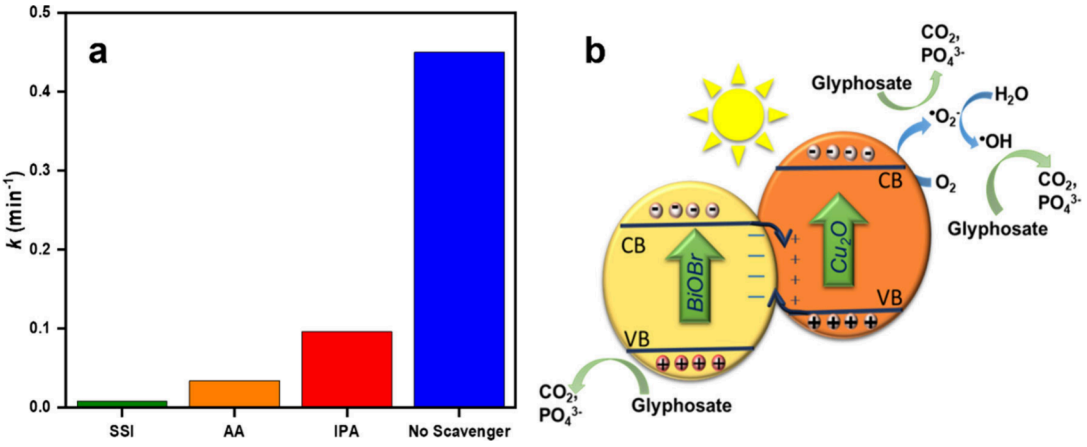

Figure 6. (a) Scavenging analysis of BiOBr/Cu_2O (**B**) for the degradation of glyphosate. (b) Schematic illustration of the proposed mechanism of degradation of glyphosate by BiOBr/Cu_2O (**B**).

insignificant decrease in glyphosate concentration was observed in the absence of the BiOBr/Cu_2O (**B**) nanocomposite under light irradiation. The single-component Cu_2O and BiOBr photocatalysts exhibited 19% and 36% degradation of glyphosate within 10 min of simulated sunlight exposure, with rate constants of 0.037 ± 0.002 min^{-1} and 0.080 ± 0.001 min^{-1}, respectively. However, the BiOBr/Cu_2O (**B**) photocatalyst demonstrated substantial activity with 100% degradation of glyphosate in 10 min of irradiation with a rate constant k of 0.450 ± 0.017 min^{-1}, which is 5 and 12 times faster than pure BiOBr and Cu_2O (Figure 5b,c). This nanocomposite photocatalyst displayed excellent photocatalytic degradation reactivity compared to previously reported materials used in the degradation of glyphosate (Table 1).

The photocatalytic degradation of glyphosate mainly occurs through two major pathways.[47] The sarcosine pathway is based on the cleavage of the C−P bond, while the AMPA pathway begins with the cleavage at the C−N bond.[47,48] Both pathways often result in a continuous loss of phosphate as glyphosate is degraded to produce carbon dioxide, phosphate, and ammonia as the mineralization products. The cleavage of the C−N to produce AMPA and glycosylic acid is more energy-favorable, and AMPA is more stable than glyphosate, which takes more time to mineralize.[48] However, low levels of AMPA were observed in the degradation of glyphosate by BiOBr/Cu_2O (**B**) photocatalyst, suggesting concurrent degradation of the emerged AMPA. To investigate this hypothesis, we conducted the light-activated degradation of AMPA as a starting material by BiOBr/Cu_2O (**B**) photocatalyst. The BiOBr/Cu_2O (**B**) nanocomposite demonstrated >90% degradation of AMPA in 15 min with a rate of 0.155 ± 0.004 min^{-1} (Figure 5c). The complete mineralization of glyphosate proceeds via the loss of a phosphate ion from AMPA to generate methylamine, which disintegrates into ammonia and CO_2. To evaluate the mineralization of glyphosate by the BiOBr/Cu_2O (**B**) nanocomposite, total organic carbon (TOC) was used to analyze for the elimination of organic carbon and formation of CO_2, while molybdenum blue analysis was used to determine the formation of phosphate. Figure S8a of the Supporting Information shows the results demonstrating that the BiOBr/Cu_2O (**B**) photocatalyst eliminated 82% of TOC in glyphosate within 180 min of the reaction. The TOC elimination results are consistent with the 80% phosphate generation determined by the molybdenum blue analysis after 180 min of the photocatalytic reaction (Figure S8b). These results establish that the BiOBr/Cu_2O (**B**) composite significantly mineralizes glyphosate compared to the pure Cu_2O and BiOBr photocatalysts.

Previous reports have demonstrated that Cu_2O semiconductors tend to suffer photo corrosion due to the onset of the Cu^+/Cu^{2+} oxidation potential within the band gap.[49] Therefore, to investigate the effect of heterojunction on the stability of the BiOBr/Cu_2O nanocomposite photocatalyst, we evaluated the activity of the material in the photocatalytic degradation of glyphosate for five consecutive cycles. As shown in Figure 5d, the BiOBr/Cu_2O photocatalyst maintained 54% activity after 5 cycles, suggesting that the heterojunction improves the electron−hole pair separation and decreases the material's photocorrosion rate.

To further determine the stability of the as-prepared photocatalysts, the recycled BiOBr/Cu_2O nanocomposites were collected and further characterized by FT-IR and TEM.

https://doi.org/10.1021/acsomega.4c07304
ACS Omega 2024, 9, 48512−48523

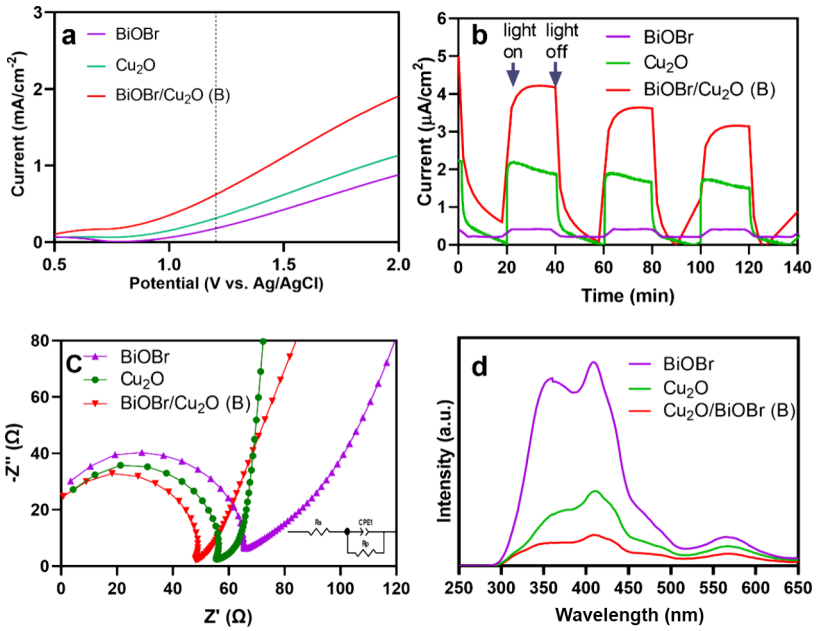

Figure 7. (a) LSV of pure Cu_2O, BiOBr, and Cu_2O/BiOBr (**B**) composite. (b) Photocurrent density of bare Cu_2O, BiOBr, and Cu_2O/BiOBr (**B**) composite. (c) PEIS analysis of bare Cu_2O, BiOBr, and Cu_2O/BiOBr (**B**) composite. (d) PL spectra of bare Cu_2O, BiOBr, and Cu_2O/BiOBr (**B**) composite.

In Figure S9a the FT-IR survey spectra of the BiOBr/Cu_2O nanocomposites before and after employing the nanocomposite in photocatalytic degradation of glyphosate for five cycles were identical. Additionally, in Figure S9b no significant differences were observed in the TEM micrographs of the unused and used material. These findings suggest that the materials maintained their structure and chemical compositions after multiple runs of photocatalytic degradation of glyphosate, indicating high stability and reusability properties of the BiOBr/Cu_2O nanocomposites.

3.4. Mechanistic Studies. The BiOBr/Cu_2O (**B**) heterojunction nanocomposite demonstrated substantial activity in the photocatalytic degradation of glyphosate. To determine the active species responsible for the degradation of glyphosate, sodium sulfite (SSI), ascorbic acid (AA), and isopropyl alcohol (IPA) were added to the photocatalytic reaction to scavenge holes (h^+), superoxide radicals ($^{\bullet}O_2^-$), and hydroxyl radicals ($^{\bullet}OH$), respectively. Figure 6a shows that the rate of degradation decreased by 98%, 93%, and 78% in the presence of SSI, AA, and IPA, respectively. These results indicate that the h^+, $^{\bullet}O_2^-$, and $^{\bullet}OH$ radicals were actively driving the degradation of glyphosate by BiOBr/Cu_2O (**B**). Based on these findings, we propose that Cu_2O and BiOBr photocatalysts are interfaced with band gap alignment in an S-scheme heterojunction (Figure 6b).[31] To elucidate this mechanism, we obtained Mott−Schottky measurements for Cu_2O and BiOBr nanostructures (Figure S10a, b), and the flat band potentials (Vfb) were estimated and used to determine the conduction band (CB) and valence band (VB) of both materials. The Cu_2O photocatalyst displayed a negative slope with a flat band potential (V_{fb}) of 1.29 V vs RHE. The valence band (VB) potentials of semiconductors with negative slope are generally more positive than the V_{fb} by ∼0.1 to 0.3 V. Therefore, the VB of Cu_2O is estimated to be 1.59 V vs RHE and the calculated value for the CB of Cu_2O is −0.80 V vs RHE from the equation CB = VB − E_g, where E_g of Cu_2O is 2.39 eV from DRS measurement.[55] Conversely, Figure S10b shows that the BiOBr has a positive slope with a V_{fb} of −0.09 V vs RHE. The space between the bottom of the conduction band and the V_{fb} of the positive slope semiconductor is negligible. Thus, the V_{fb} value can be taken as the CB of BiOBr, and the VB is calculated to be 2.77 V vs RHE from DRS measurement.[35,56] Based on the calculations and the data presented in Figure 6b, it is evident that Cu_2O has a lower work function and higher conduction band (CB) and valence band (VB) positions compared to BiOBr. As a result, Cu_2O serves as the reductive photocatalyst (RP), while BiOBr acts as the oxidative photocatalyst (OP).[34] Thus, upon contact in a heterojunction, electrons diffuse freely from Cu_2O to BiOBr, creating an electron depletion layer and an electron accumulation layer near the interface in RP and OP, respectively.[31] Simultaneously, an internal electric field is generated within the space charge region of Cu_2O and BiOBr and the Fermi energy levels equilibrate, and BiOBr becomes negatively charged, while Cu_2O is positively charged.[57] The band bends to facilitate the flow of the photoexcited electrons from the CB of BiOBr to the VB of Cu_2O, leading to the recombination of photogenerated electrons and holes at the interface due to low redox abilities and Coulombic attraction. The combined effect of the internal electric field, band bending, and Coulombic attraction causes the electrons and holes with weak redox potentials to recombine, allowing the photoexcited carriers with strong redox abilities available for reactions.[34] Consequently, as shown in Figure 6b, when photon energy is absorbed, double simultaneous excitation occurs on Cu_2O and BiOBr, allowing electrons to move from the valence band (VB) to the conduction band (CB) of both photocatalysts. In Cu_2O, the electrons in the CB are free to interact with molecular oxygen to produce superoxide radical anions ($^{\bullet}O_2^-$), which play a crucial role in degrading glyphosate. At the same time, the holes in the VB of BiOBr are available to oxidize glyphosate directly. Furthermore, the $^{\bullet}O_2^-$ radicals can also react with hydrogen ions to generate hydroxyl radicals that degrade glyphosate.[58] Consequently, the

https://doi.org/10.1021/acsomega.4c07304
ACS Omega 2024, 9, 48512−48523

S-scheme heterojunction architecture increases the separation of electrons and holes and expands the redox potentials, thereby enhancing the photocatalytic activity of the nanocomposite to mineralize glyphosate by superoxide radical anions, $^{\bullet}O_2^-$, hydroxyl radicals ($^{\bullet}OH$), and holes, h^+.

3.5. Photoelectrochemical and Photoluminescence Studies. Linear sweep voltammetry (LSV), photocurrent response, photoelectrochemical impedance spectroscopy (PEIS), and photoluminescence (PL) spectroscopy were conducted to investigate the charge carriers' dynamics and the photoexcited electrons/holes separation. The LSV data in Figure 7a provides information about the photocurrent densities of different materials. The LSV plot in Figure 7a confirms that the BiOBr/Cu_2O heterojunction nanocomposite has the highest photocurrent density of 0.62 mA/cm^2 at 1.20 V vs Ag/AgCl (0.58 V vs RHE) in comparison to the single photocatalysts BiOBr and Cu_2O. This data is consistent with the high photocurrent density that was demonstrated by BiOBr/Cu_2O (**B**) nanocomposite photoelectrode in the photocurrent response studies when compared to pure Cu_2O and BiOBr photocatalysts (Figure 7b). The LSV and photocurrent response analysis confirms the positive influence of heterojunction design in enhancing the separation efficiency of the electron/hole pair. These results corroborate the substantial photocatalytic activity demonstrated by BiOBr/Cu_2O (**B**) heterojunction compared to the individual photocatalysts.

Figure 7c displays the PEIS spectra of all the materials and a similar trend is detected as in the photocurrent response studies. The BiOBr/Cu_2O (**B**) heterojunction nanocomposite displayed the smallest arc (Figure 7c) compared to the pure Cu_2O and BiOBr photocatalysts. The equivalent circuits were derived from the PEIS of the Cu_2O, BiOBr, and BiOBr/Cu_2O (**B**) nanocomposite electrode using the Randles method (Figure 7c inset) to evaluate the effect of heterojunction on the overall series resistance (Rs) and interfacial charge transfer resistance (Rp) of the photocatalyst. The BiOBr/Cu_2O (**B**) exhibited a small Rs and Rp value at 39.07 Ω and 1.71 × 10^3 Ω compared to the bare Cu_2O (71.52 Ω and 1.45 × 10^4 Ω), and BiOBr (44.11 Ω and 4.23 × 10^4 Ω) values, indicating enhanced electron/hole separation by the heterojunction BiOBr/Cu_2O (**B**) photocatalyst. This hypothesis is further corroborated by the PL analysis (Figure 7d). The Cu_2O/BiOBr (**B**) nanocomposite demonstrated much lower PL emission at 430 nm than the bare Cu_2O and BiOBr photocatalysts, implying the effect of interfacing the two metal oxides on the rate of charge carriers' recombination. Taking together, these results indicate that the creation of an S-scheme heterojunction between Cu_2O and BiOBr in the Cu_2O/BiOBr nanocomposite decreases the rate of e^-/h^+ recombination and facilitates the transfer of charge carriers to the surface of the photocatalyst, which leads to a significant increase in the photocatalytic activity.

4. CONCLUSION

We developed a facial low-temperature hydrothermal method to synthesize BiOBr/Cu_2O heterojunction nanocomposite. Manipulating the synthesis conditions and precursors significantly influenced the extent of interfacial integration of the BiOBr and Cu_2O metal oxides. The optimized BiOBr/Cu_2O heterojunction nanocomposite demonstrated high activity in the photocatalytic degradation of the cationic and anionic days, rhodamine B and methyl orange, respectively, under visible light irradiation. The BiOBr/Cu_2O nanocomposite displayed rapid photocatalytic mineralization of glyphosate and AMPA. The improved activity is attributed to the high surface area, unique morphology, and the S-scheme heterojunction of the composite material, which enhances the separation of charge carriers and increases the redox potential of the electrons and holes. These results suggest that the rational design of metal oxide heterojunctions promises the application of the degradation of a wide range of emerging organic contaminants.

■ ASSOCIATED CONTENT

Supporting Information

The Supporting Information is available free of charge at https://pubs.acs.org/doi/10.1021/acsomega.4c07304.

HRTEM micrograph of the BiOBr/Cu_2O (B) composite material; TEM micrographs of BiOBr/Cu_2O (A) and BiOBr/Cu_2O (C); EDS spectra of the BiOBr/Cu_2O (B) composite material; N_2−BET adsorption−desorption isotherm and pore size distribution plots of the materials; Table showing BET surface area of the samples; additional XPS spectra of the materials; UV-DRS spectra for BiOBr/Cu_2O (A) and BiOBr/Cu_2O (C); TOC elimination of glyphosate by the BiOBr/Cu_2O (B) photocatalyst and % phosphate formation of BiOBr/Cu_2O (B); FT-IR of BiOBr/Cu_2O before and after five cycles of degradation; TEM micrographs of BiOBr/Cu_2O before and after five cycles of degradation; Mott−Schottky curve for (a) Cu_2O and (b) BiOBr (PDF)

■ AUTHOR INFORMATION

Corresponding Author

Elsayed M. Zahran − *Department of Chemistry, Ball State University, Muncie, Indiana 47306, United States;* orcid.org/0000-0003-3456-515X; Email: zahran@bsu.edu

Authors

Albert Gonzalez − *Department of Chemistry, Ball State University, Muncie, Indiana 47306, United States*

Abelline Fionah − *Department of Chemistry, Ball State University, Muncie, Indiana 47306, United States;* Present Address: Department of Chemistry, University of Kentucky, Lexington, KY 40506, USA

Gbemisola J. Bamiduro − *Department of Chemistry, Ball State University, Muncie, Indiana 47306, United States;* orcid.org/0000-0002-6515-6087

Complete contact information is available at: https://pubs.acs.org/10.1021/acsomega.4c07304

Author Contributions

#A.G., A.F., and G.J.B. contributed equally and shared the first author.

Notes

The authors declare no competing financial interest.

■ ACKNOWLEDGMENTS

We acknowledge partial funding for this work from the National Science Foundation, the Indiana Academy of Science, and Ball State University. We thank Dr. Yaroslav Losovyj at the Nanoscale Characterization Facility, Department of Chemistry, Indiana University, for helping with the XPS measurements

and Dr. Dali Qin at the Electron Microscopy Center, University of Kentucky, for helping with the HRTEM analysis.

REFERENCES

(1) Hu, A.; Zhang, X.; Luong, D.; Oakes, K. D.; Servos, M. R.; Liang, R.; Kurdi, S.; Peng, P.; Zhou, Y. Adsorption and Photocatalytic Degradation Kinetics of Pharmaceuticals by TiO_2 Nanowires During Water Treatment. *Waste and Biomass Valorization* **2012**, *3* (4), 443−449.

(2) Lapworth, D. J.; Baran, N.; Stuart, M. E.; Ward, R. S. Emerging organic contaminants in groundwater: A review of sources, fate and occurrence. *Environ. Pollut.* **2012**, *163*, 287−303.

(3) Bradberry, S. M.; Proudfoot, A. T.; Vale, J. A. Glyphosate Poisoning. *Toxicological Reviews* **2004**, *23* (3), 159−167.

(4) Samsel, A.; Seneff, S. Glyphosate, Pathways to Modern Diseases II: Celiac Sprue and Gluten Intolerance. *Interdiscip Toxicol* **2013**, *6* (4), 159−84.

(5) Samsel, A.; Seneff, S. Glyphosate, pathways to modern diseases III: Manganese, neurological diseases, and associated pathologies. *Surg Neurol Int.* **2015**, *6*, 45.

(6) Battaglin, W. A.; Meyer, M. T.; Kuivila, K. M.; Dietze, J. E. Glyphosate and Its Degradation Product AMPA Occur Frequently and Widely in U.S. Soils, Surface Water, Groundwater, and Precipitation. *JAWRA Journal of the American Water Resources Association* **2014**, *50* (2), 275−290.

(7) Soares, D.; Silva, L.; Duarte, S.; Pena, A.; Pereira, A. Glyphosate Use, Toxicity and Occurrence in Food. *Foods* **2021**, *10* (11), 2785.

(8) Cosemans, C.; Van Larebeke, N.; Janssen, B. G.; Martens, D. S.; Baeyens, W.; Bruckers, L.; Den Hond, E.; Coertjens, D.; Nelen, V.; Schoeters, G.; Hoppe, H.-W.; Wolfs, E.; Smeets, K.; Nawrot, T. S.; Plusquin, M. Glyphosate and AMPA exposure in relation to markers of biological aging in an adult population-based study. *International Journal of Hygiene and Environmental Health* **2022**, *240*, 113895.

(9) Bamiduro, G. J.; Dollar, C. M.; Abaddi, S.; Ensinger, N.; Zahran, E. M. Rapid Photocatalytic Mineralization of Glyphosate by Pd@ $BiVO_4$/BiOBr Nanosheets: Mechanistic Studies and Degradation Pathways. *Catal. Commun.* **2023**, *174*, 106599.

(10) Mickey, C. D. Solar photovoltaic cells. *J. Chem. Educ.* **1981**, *58* (5), 418.

(11) Khan, M. M.; Adil, S. F.; Al-Mayouf, A. Metal oxides as photocatalysts. *Journal of Saudi Chemical Society* **2015**, *19* (5), 462−464.

(12) Chowdhury, P.; Malekshoar, G.; Ray, A. K. Dye-Sensitized Photocatalytic Water Splitting and Sacrificial Hydrogen Generation: Current Status and Future Prospects. *Inorganics* **2017**, *5* (2), 34.

(13) Li, X.; Yu, J.; Jaroniec, M. Hierarchical Photocatalysts. *Chem. Soc. Rev.* **2016**, *45* (9), 2603−2636.

(14) Humayun, M.; Raziq, F.; Khan, A.; Luo, W. Modification Strategies of TiO_2 for Potential Applications in Photocatalysis: a Critical Review. *Green Chemistry Letters and Reviews* **2018**, *11* (2), 86−102.

(15) Lv, Y.-R.; Liu, C.-J.; He, R.-K.; Li, X.; Xu, Y.-H. BiVO4/TiO2 heterojunction with enhanced photocatalytic activities and photoelectochemistry performances under visible light illumination. *Mater. Res. Bull.* **2019**, *117*, 35−40.

(16) Park, B. H.; Park, H.; Kim, T.; Yoon, S. J.; Kim, Y.; Son, N.; Kang, M. S-scheme assisted Cu2O/ZnO flower-shaped heterojunction catalyst for breakthrough hydrogen evolution by water splitting. *Int. J. Hydrogen Energy* **2021**, *46* (77), 38319−38335.

(17) Wang, H.; Zhang, L.; Chen, Z.; Hu, J.; Li, S.; Wang, Z.; Liu, J.; Wang, X. Semiconductor Heterojunction Photocatalysts: Design, Construction, and Photocatalytic Performances. *Chem. Soc. Rev.* **2014**, *43* (15), 5234−5244.

(18) Hacialioglu, S.; Meng, F.; Jin, S. Facile and Mild Solution Synthesis of Cu_2O Nanowires and Nanotubes Driven by Screw Dislocations. *Chem. Commun.* **2012**, *48* (8), 1174−1176.

(19) Xiong, L.; Yu, H.; Nie, C.; Xiao, Y.; Zeng, Q.; Wang, G.; Wang, B.; Lv, H.; Li, Q.; Chen, S. Size-Controlled Synthesis of Cu_2O Nanoparticles: Size Effect on Antibacterial Activity and Application as a Photocatalyst for Highly Efficient H_2O_2 Evolution. *RSC Adv.* **2017**, *7* (82), 51822−51830.

(20) Liang, X.; Gao, L.; Yang, S.; Sun, J. Facile Synthesis and Shape Evolution of Single-Crystal Cuprous Oxide. *Adv. Mater.* **2009**, *21* (20), 2068−2071.

(21) Kuo, C.-H.; Yang, Y.-C.; Gwo, S.; Huang, M. H. Facet-Dependent and Au Nanocrystal-Enhanced Electrical and Photocatalytic Properties of Au−Cu_2O Core−Shell Heterostructures. *J. Am. Chem. Soc.* **2011**, *133* (4), 1052−1057.

(22) Zheng, Z.; Huang, B.; Wang, Z.; Guo, M.; Qin, X.; Zhang, X.; Wang, P.; Dai, Y. Crystal Faces of Cu_2O and their Stabilities in Photocatalytic Reactions. *J. Phys. Chem. C* **2009**, *113* (32), 14448−14453.

(23) Koiki, B. A.; Arotiba, O. A. Cu_2O as an Emerging Semiconductor in Photocatalytic and Photoelectrocatalytic Treatment of Water Contaminated with Organic Substances: A Review. *RSC Adv.* **2020**, *10* (60), 36514−36525.

(24) He, X.; Kai, T.; Ding, P. Heterojunction Photocatalysts for Degradation of the Tetracycline Antibiotic: A Review. *Environ. Chem. Lett.* **2021**, *19* (6), 4563−4601.

(25) Ge, J.; Zhang, Y.; Heo, Y.-J.; Park, S.-J. Advanced Design and Synthesis of Composite Photocatalysts for the Remediation of Wastewater: A Review. *Catalysts* **2019**, *9* (2), 122.

(26) Clarizia, L.; Russo, D.; Di Somma, I.; Andreozzi, R.; Marotta, R. Hydrogen Generation through Solar Photocatalytic Processes: A Review of the Configuration and the Properties of Effective Metal-Based Semiconductor Nanomaterials. *Energies* **2017**, *10* (10), 1624.

(27) Hu, S.; Zhou, F.; Wang, L.; Zhang, J. Preparation of Cu_2O/CeO_2 Heterojunction Photocatalyst for the Degradation of Acid Orange 7 under Visible Light Irradiation. *Catal. Commun.* **2011**, *12* (9), 794−797.

(28) Wang, Z.; Chu, Z.; Dong, C.; Wang, Z.; Yao, S.; Gao, H.; Liu, Z.; Liu, Y.; Yang, B.; Zhang, H. Ultrathin BiOX (X = Cl, Br, I) Nanosheets with Exposed {001} Facets for Photocatalysis. *ACS Applied Nano Materials* **2020**, *3* (2), 1981−1991.

(29) Ganose, A. M.; Cuff, M.; Butler, K. T.; Walsh, A.; Scanlon, D. O. Interplay of Orbital and Relativistic Effects in Bismuth Oxyhalides: BiOF, BiOCl, BiOBr, and BiOI. *Chem. Mater.* **2016**, *28* (7), 1980−1984.

(30) Pálmai, M.; Zahran, E. M.; Angaramo, S.; Bálint, S.; Pászti, Z.; Knecht, M. R.; Bachas, L. G. Pd-decorated m-$BiVO_4$/BiOBr Ternary Composite with Dual Heterojunction for Enhanced Photocatalytic Activity. *Journal of Materials Chemistry A* **2017**, *5* (2), 529−534.

(31) Xu, Q.; Zhang, L.; Cheng, B.; Fan, J.; Yu, J. S-Scheme Heterojunction Photocatalyst. *Chem.* **2020**, *6* (7), 1543−1559.

(32) Fu, J.; Xu, Q.; Low, J.; Jiang, C.; Yu, J. Ultrathin 2D/2D WO_3/g-C_3N_4 Step-Scheme H_2-Production Photocatalyst. *Applied Catalysis B: Environmental* **2019**, *243*, 556−565.

(33) Wang, Z.; Chen, Y.; Zhang, L.; Cheng, B.; Yu, J.; Fan, J. Step-Scheme CdS/TiO_2 Nanocomposite Hollow Microsphere with Enhanced Photocatalytic CO_2 Reduction Activity. *Journal of Materials Science & Technology* **2020**, *56*, 143−150.

(34) Zhang, H.; Liu, J.; Zhang, Y.; Cheng, B.; Zhu, B.; Wang, L. BiOBr/COF S-scheme Photocatalyst for H_2O_2 Production via Concerted Two-Electron Pathway. *Journal of Materials Science & Technology* **2023**, *166*, 241−249.

(35) Bamiduro, G. J.; Zahran, E. M. Pd@$Bi_2Ru_2O_7$/$BiVO_4$ Z-Scheme Heterojunction Nanocomposite Photocatalyst for the Degradation of Trichloroethylene. *ACS Appl. Mater. Interfaces* **2023**, *15* (51), 59337−59347.

(36) Plascencia-Hernández, F.; Luna, A. L.; Colbeau-Justin, C.; Santiago, P.; Garcia-Rocha, M.; Valverde-Aguilar, G.; Valenzuela, M. A. Cu_2O Cubic and Polyhedral Structures versus Commercial Powder: Shape Effect on Photocatalytic Activity under Visible Light. *Journal of Saudi Chemical Society* **2019**, *23* (8), 1016−1023.

(37) Ma, Q.; Chen, Q. EPR, DFT, and Mott−Schottky Study on Visible Light Photocatalytic Activity of Au and Co_3O_4 Mediated Bi_2WO_6: Role of SPR and Multi-Valence States. *Journal of Materials Science: Materials in Electronics* **2022**, *33* (27), 21363−21383.

https://doi.org/10.1021/acsomega.4c07304
ACS Omega 2024, 9, 48512−48523

(38) Ho, W. C. J.; Tay, Q.; Qi, H.; Huang, Z.; Li, J.; Chen, Z. Photocatalytic and Adsorption Performances of Faceted Cuprous Oxide (Cu_2O) Particles for the Removal of Methyl Orange (MO) from Aqueous Media. *Molecules* **2017**, *22* (4), 677.
(39) Kannan, S.; Subiramaniyam, N. P.; Sathishkumar, M. A Novel Green Synthesis Approach for Improved Photocatalytic Activity and Antibacterial Properties of Zinc Sulfide Nanoparticles using Plant Extract of Acalypha Indica and Tridax Procumbens. *Journal of Materials Science: Materials in Electronics* **2020**, *31* (12), 9846−9859.
(40) Olagunju, M. O.; Zahran, E. M.; Reed, J. M.; Zeynaloo, E.; Shukla, D.; Cohn, J. L.; Surnar, B.; Dhar, S.; Bachas, L. G.; Knecht, M. R. Halide Effects in $BiVO_4$/BiOX Heterostructures Decorated with Pd Nanoparticles for Photocatalytic Degradation of Rhodamine B as a Model Organic Pollutant. *ACS Applied Nano Materials* **2021**, *4* (3), 3262−3272.
(41) Han, A.; Zhang, H.; Chuah, G.-K.; Jaenicke, S. Influence of the Halide and Exposed Facets on the Visible-Light Photoactivity of Bismuth Oxyhalides for Selective Aerobic Oxidation of Primary Amines. *Applied Catalysis B: Environmental* **2017**, *219*, 269−275.
(42) Su, Y.; Li, H.; Ma, H.; Robertson, J.; Nathan, A. Controlling Surface Termination and Facet Orientation in Cu(2)O Nanoparticles for High Photocatalytic Activity: A Combined Experimental and Density Functional Theory Study. *ACS Appl. Mater. Interfaces* **2017**, *9* (9), 8100−8106.
(43) Chen, T. N.; Kao, J. C.; Zhong, X. Y.; Chan, S. J.; Patra, A. S.; Lo, Y. C.; Huang, M. H. Facet-Specific Photocatalytic Activity Enhancement of Cu(2)O Polyhedra Functionalized with 4-Ethynylanaline Resulting from Band Structure Tuning. *ACS Cent Sci.* **2020**, *6* (6), 984−994.
(44) Li, H.; Cao, X.; Zhang, C.; Yu, Q.; Zhao, Z.; Niu, X.; Sun, X.; Liu, Y.; Ma, L.; Li, Z. Enhanced Adsorptive Removal of Anionic and Cationic Dyes from Single or Mixed Dye Solutions using MOF PCN-222. *RSC Adv.* **2017**, *7* (27), 16273−16281.
(45) Self, K.; Zhou, W. Surface Charge Driven Growth of Eight-Branched Cu_2O Crystals. *Cryst. Growth Des.* **2016**, *16* (9), 5377−5384.
(46) Wang, D.; Shen, H.; Guo, L.; Wang, C.; Fu, F. Porous BiOBr/Bi_2MoO_6 Heterostructures for Highly Selective Adsorption of Methylene Blue. *ACS Omega* **2016**, *1* (4), 566−577.
(47) Jaisi, D. P.; Li, H.; Wallace, A. F.; Paudel, P.; Sun, M.; Balakrishna, A.; Lerch, R. N. Mechanisms of Bond Cleavage during Manganese Oxide and UV Degradation of Glyphosate: Results from Phosphate Oxygen Isotopes and Molecular Simulations. *J. Agric. Food Chem.* **2016**, *64* (45), 8474−8482.
(48) Cao, L.; Ma, D.; Zhou, Z.; Xu, C.; Cao, C.; Zhao, P.; Huang, Q. Efficient photocatalytic degradation of herbicide glyphosate in water by magnetically separable and recyclable BiOBr/Fe3O4 nanocomposites under visible light irradiation. *Chemical Engineering Journal* **2019**, *368*, 212−222.
(49) Zahran, E. M.; Bedford, N. M.; Nguyen, M. A.; Chang, Y. J.; Guiton, B. S.; Naik, R. R.; Bachas, L. G.; Knecht, M. R. Light-Activated Tandem Catalysis Driven by Multicomponent Nanomaterials. *J. Am. Chem. Soc.* **2014**, *136* (1), 32−35.
(50) Tang, Q. Y.; Yang, M. J.; Yang, S. Y.; Xu, Y. H. Enhanced Photocatalytic Degradation of Glyphosate over 2D CoS/BiOBr Heterojunctions under Visible Light Irradiation. *J. Hazard Mater.* **2021**, *407*, 124798.
(51) Tang, Q.-Y.; Huo, R.; Ou, L.-Y.; Luo, X.-L.; Lv, Y.-R.; Xu, Y.-H. One-Pot Synthesis of Peony-Like Bi_2S_3/$BiVO_4$(040) with High Photocatalytic Activity for Glyphosate Degradation under Visible Light Irradiation. *Chinese Journal of Catalysis* **2019**, *40* (4), 580−589.
(52) Luo, X. L.; Chen, Z. Y.; Yang, S. Y.; Xu, Y. H. Two-Step Hydrothermal Synthesis of Peanut-Shaped Molybdenum Diselenide/Bismuth Vanadate ($MoSe_2$/$BiVO_4$) with Enhanced Visible-Light Photocatalytic Activity for the Degradation of Glyphosate. *J. Colloid Interface Sci.* **2018**, *532*, 456−463.
(53) Lv, Y. R.; He, R. K.; Chen, Z. Y.; Li, X.; Xu, Y. H. Fabrication of Hierarchical Copper Sulfide/Bismuth Tungstate p-n Heterojunction with Two-Dimensional (2D) Interfacial Coupling for Enhanced Visible-Light Photocatalytic Degradation of Glyphosate. *J. Colloid Interface Sci.* **2020**, *560*, 293−302.
(54) Wu, H.; Sun, Q.; Chen, J.; Wang, G.-Y.; Wang, D.; Zeng, X.-F.; Wang, J.-X. Citric Acid-Assisted Ultrasmall CeO_2 Nanoparticles for Efficient Photocatalytic Degradation of Glyphosate. *Chemical Engineering Journal* **2021**, *425*, 130640.
(55) Luo, L.; Zhang, T.; Zhang, X.; Yun, R.; Lin, Y.; Zhang, B.; Xiang, X. Enhanced Hydrogen Production from Ethanol Photoreforming by Site-Specific Deposition of Au on Cu_2O/TiO_2 p-n Junction. *Catalysts* **2020**, *10* (5), 539.
(56) Shao, P.-W.; Siao, Y.-S.; Lai, Y.-H.; Hsieh, P.-Y.; Tsao, C.-W.; Lu, Y.-J.; Chen, Y.-C.; Hsu, Y.-J.; Chu, Y.-H. Flexible $BiVO_4$/WO_3/ITO/Muscovite Heterostructure for Visible-Light Photoelectrochemical Photoelectrode. *ACS Appl. Mater. Interfaces* **2021**, *13* (18), 21186−21193.
(57) Luo, C.; Long, Q.; Cheng, B.; Zhu, B.; Wang, L. A DFT Study On S-Scheme Heterojunction Consisting of Pt Single Atom Loaded G-C_3N_4 and BiOCl for Photocatalytic CO_2 Reduction. *Acta Physico Chimica Sinica* **2023**, *0* (0), 2212026−0.
(58) Siahrostami, S.; Li, G.-L.; Viswanathan, V.; Norskov, J. K. One- or Two-Electron Water Oxidation, Hydroxyl Radical, or H_2O_2 Evolution. *J. Phys. Chem. Lett.* **2017**, *8* (6), 1157−1160.

https://doi.org/10.1021/acsomega.4c07304
ACS Omega 2024, 9, 48512−48523